

## A shear and plantar pressure sensor based on fiber-optic bend loss

---

**Wei-Chih Wang, PhD;<sup>1\*</sup> William R. Ledoux, PhD;<sup>1–3</sup> Bruce J. Sangeorzan, MD;<sup>2–3</sup> Per G. Reinhall, PhD<sup>1</sup>**  
*Departments of <sup>1</sup>Mechanical Engineering and <sup>2</sup>Orthopaedics and Sports Medicine, University of Washington, Seattle, WA; <sup>3</sup>Department of Veterans Affairs (VA) Rehabilitation Research and Development, Center of Excellence for Limb Loss Prevention and Prosthetic Engineering, VA Puget Sound Health Care System, Seattle, WA*

**Abstract**—Lower-limb complications associated with diabetes include the development of plantar ulcers that can lead to infection and subsequent amputation. While we know from force-plate analyses that medial/lateral and anterior/posterior shear components of ground-reaction forces exist, little is known about the actual distribution of these stresses during daily activities or about the role that shear stresses play in causing plantar ulceration. Furthermore, one critical reason why these data have not been obtained previously is the lack of a validated, widely used, commercially available shear sensor, partly because of the various technical issues associated with measuring shear. In this study, we present a novel means of transducing plantar pressure and shear stress with a fiber-optic sensor. The pressure/shear sensor consists of an array of optical fibers lying in perpendicular rows and columns separated by elastomeric pads. We constructed a map of normal and shear stresses based on observed macrobending through the intensity attenuation from the physical deformation of two adjacent perpendicular fibers. Initial results show that this sensor exhibits low noise and responds to applied normal and shear loads with good repeatability.

**Key words:** anterior/posterior shear, biomechanics, biosensing techniques, diabetes mellitus, foot ulcers, gait, lower-limb complications, plantar pressure, plantar ulcers, ulcer.

### INTRODUCTION

Diabetes mellitus is a disease that affects the lives of millions of people. Lower-limb complications associated with diabetes include developing plantar ulcers, which

can lead to infection and subsequent amputation. Although plantar ulcers have been associated with several factors—including, but not limited to, arterial insufficiency or peripheral vascular disease, peripheral neuropathy, and musculoskeletal abnormalities [1]—we now understand that most foot ulcers are caused by mechanical trauma to an insensate foot [2]. Plantar pressure, or repetitive stress, has been associated with the development of ulcers [3–5]. Others have postulated that shear stress is an important component of ulcer development [6–8]. Unfortunately, the exact role that shear stress plays in plantar ulceration is not completely understood, mostly because shear stress has not been quantitatively studied in a wide-scale manner. One additional reason why data have not been obtained previously is the lack of a validated, widely used, commercially available shear sensor.

---

**Abbreviations:** LED = light-emitting diode, LVDT = linear variable displacement transducer, 2-D = two-dimensional, 3-D = three-dimensional.

**This work was supported in part by the Department of Veterans Affairs, Rehabilitation Research and Development Service, grants A0806C and A2661C.**

\*Address all correspondence to Wei-Chih Wang, PhD; Department of Mechanical Engineering, University of Washington, Seattle, WA 98195; (206) 543-2479; fax: (206) 685-8047. Email: abong@u.washington.edu

DOI: 10.1682/JRRD.2004.07.0076

Others have developed shear sensors based on various technologies. Lord et al. have measured shear stress at point locations with magneto-resistive transducer disks (16 mm in diameter and 3 mm thick) mounted in an insole that is directly placed under three critical stress regions under a foot (e.g., heel and first and third metatarsals) [9]. The sensor's resistance varies with the strength of the magnetic field in which it is placed. Lateral movement corresponding to shear force can be monitored by the movement of a magnet placed centrally above a center-tapped magneto resistor in a bridge configuration [10]. A piezoelectric film-based sensor that uses copolymer PVDF-TrFE has also been studied [11]. Again, the sensors are few in number and are placed only at critical locations. In their study, Akhlaghi and Pepper could not measure shear distribution over the plantar interface with the piezoelectric sensor [11]. More recently, developments have been made in distributive shear and pressure sensors that use an integrated-capacitive sensor [12] and strain-gauge sensor [13]. One of the problems with the capacitive sensor is its susceptibility to electrical interference because of its high impedance. Strain gauges, on the other hand, require additional structure to extract the shear component. Both designs suffer from low spatial resolution, drift, and a high sensitivity to temperature. Another severe limitation is that the materials used in these sensors are not compatible with skin when these sensors are configured to measure shear. This makes all these sensors unsuitable for use as an in-shoe shear sensor since they affect the stresses they are intended to measure.

Another means of transducing force is the use of optical fibers. Optical sensors are unaffected by electromagnetic field interference and can be made relatively compact with a diode source and detector. Optical sensors are also known for their sensitivity and high dynamic range. Furthermore, the sensors can be embedded in most structures with minimal modification. Optical sensors do not suffer from hysteresis and drift, and their response tends to be highly linear. However, no available optical sensors exist that measure pressure and shear distribution over a surface. Current optical sensors all use a single optical fiber and are intended for measuring a single point of strain or pressure [14]. We have chosen to explore the use of fiber optics as a means of transducing shear and pressure.

This paper describes the results of our initial study of a  $2 \times 2$  prototype shear sensor that uses a fiber-optic bend-loss sensor array. The sensor consists of an array of

optical fibers lying in perpendicular rows and columns separated by elastomeric pads. We generated a map of normal and shear stresses based on observed macro-bending through the intensity attenuation from the physical deformation of two adjacent perpendicular fibers.

## METHODS

The fiber-optic technique chosen for sensing shear and pressure is the bend-loss technique. The technique is simple, reliable, and effective in determining the force-induced fiber deformation. The operating principle of a fiber-based macrobend sensor depends on the transmission power loss caused by coupling between different propagating core modes and from core mode to radiation mode. Under the condition in which  $r/R\Delta$  is to remain small, the light-intensity attenuation  $\gamma_B$  is equal to [15]

$$\gamma_B = 10(\log R) \left[ \left( \frac{a+2}{2a} \right) \left( \frac{r}{R\Delta} \right) \right],$$

where  $r$  is the core radius,  $a$  specifies the shape of index of refraction (for a parabolic profile,  $a = 2$  and for a step profile,  $a = \infty$ ),  $R$  is radius of curvature of the bend, and  $\Delta$  is the relative refractive index difference between core and cladding. On the basis of this equation, the bend loss apparently can be enhanced (i.e., the intensity attenuation will increase) with a smaller refractive index difference between core and cladding or with an optical fiber with a larger core radius.

The basic configuration of the fiber-optic sensor system incorporates a mesh. (Note that pressure sensors typically measure a force over a known area and pressure is subsequently calculated. As such, our sensor measures force as well; thus, all our data are in Newtons.) This mesh comprises two sets of parallel fiber planes (**Figure 1**). The two fiber planes are configured so that the parallel rows of fibers of the top and bottom planes are perpendicular to one another. The planes are sandwiched together, creating one sensing sheet. Information from the orthogonal fibers corresponds to information on a set of orthogonal axes. This information creates a two-dimensional (2-D) plot of the pressure distribution on the mesh. For bend loss, both sets of fibers are illuminated. We can determine 2-D information by measuring the loss of light from each fiber. Knowing which fiber along the  $x$ -axis dims and which one

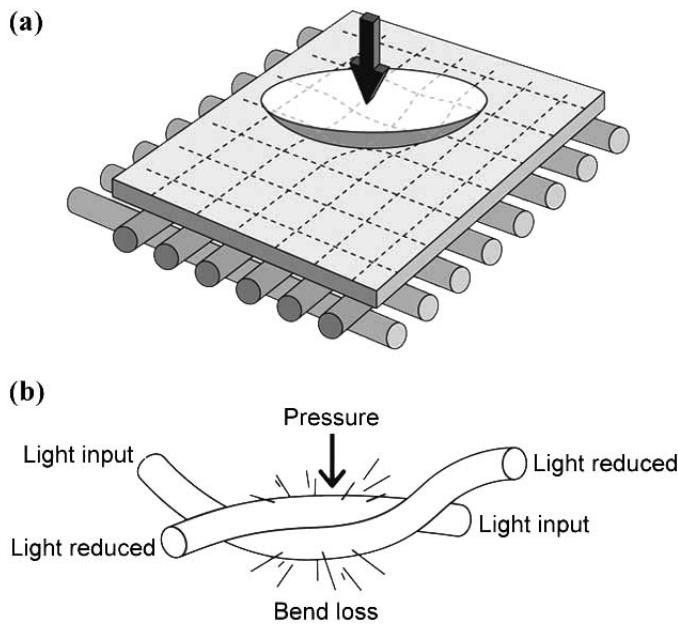


**Figure 1.** (a) Basic configuration of fiber-optic sensor systems and (b) light loss from an applied pressure.

along the  $y$ -axis dims, one can determine the  $x$ - and  $y$ -coordinates of the pressure point.

The shear sensor is constructed of two layers of bend-loss mesh sensors (**Figure 2**). The basic design is a multi-layered sensor in which the top and bottom layers are composed of a sensor mesh embedded in a high-shear-compliant shoe insole. The coordinates of the pressure points are taken from the top and bottom mesh sensors. With this method of determining shear, we assume that the pressure points are originally directly above and beneath one another. The pressure points will be shifted out of alignment because of shearing forces, and the amount of misalignment determines the amount of shear.

The prototype sensor consisted of two  $2 \times 2$  matrix arrays of fibers, in which only one array was required for measuring normal force, but two layers were required for shear (**Figure 3**). Each fiber mesh was placed between two gel/polymeric shoe insole pads. The prototype consisted of an insole layer, a fiber mesh layer, another insole layer, a second fiber mesh layer, and a final insole layer; all layers were held together by rubber cement. Fibers were secured to the elastomeric pad by strings. For each fiber layer, the intersection of a row and a column fiber formed a pressure point, with four pressure points on each layer (**Figure 4**). The separation between the two

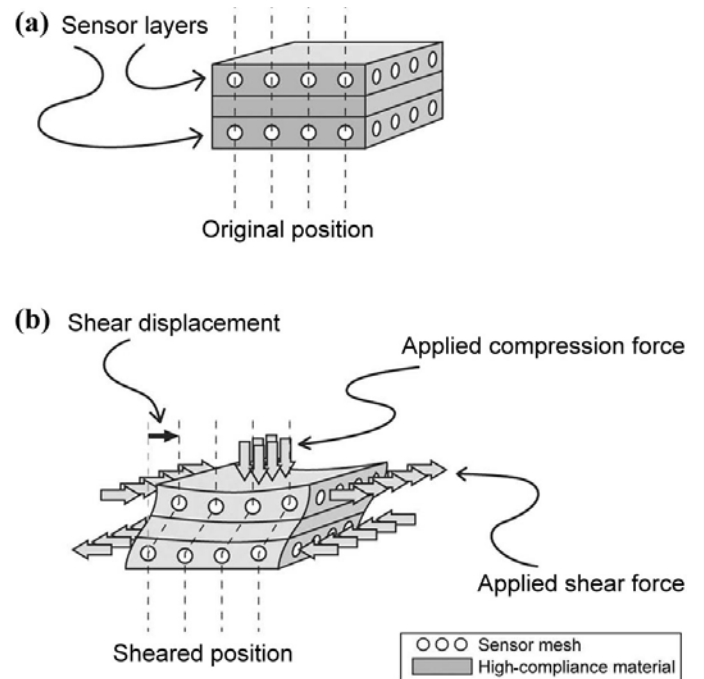


**Figure 2.** Basic design of shear-sensor configuration: (a) original position and (b) sheared position.

neighboring fibers in the  $x$ - and  $y$ -directions was 1 cm; therefore, each pressure point (“a,” “b,” “c,” and “d”) had a sensing area of  $1 \times 1 \text{ cm}^2$ , where the center of each sensing element is located at the two crossing fibers. The fiber channels on the top sensor layer were labeled with odd numbers, whereas the fiber channels on the bottom sensor layer were even numbers.

The multimode fibers have a graded refractive index, with a  $200 \text{ }\mu\text{m}$  core and  $250 \text{ }\mu\text{m}$  cladding. The fibers are powered by a  $100 \text{ mW}$  ( $\lambda_{\text{nominal}} = 850 \text{ nm}$ ) light-emitting diode (LED). The displacement of the pressure point is detected on the basis of the principle of macrobend loss. An eight-element photodetector array collects the intensity of the light transmitted through the fibers. Signals taken from the detector are fed into a data-acquisition system in which the system collects and generates a 2-D force map based on the light attenuation on the spatial distribution of macrobends. The data-acquisition system includes a National Instrument 16-input,  $500 \text{ kb/s}$ , 12-bit multifunction input/output data-acquisition card, LabVIEW software, and a laptop computer. The output intensity from the sensor provides information on the magnitude and position of the applied load.

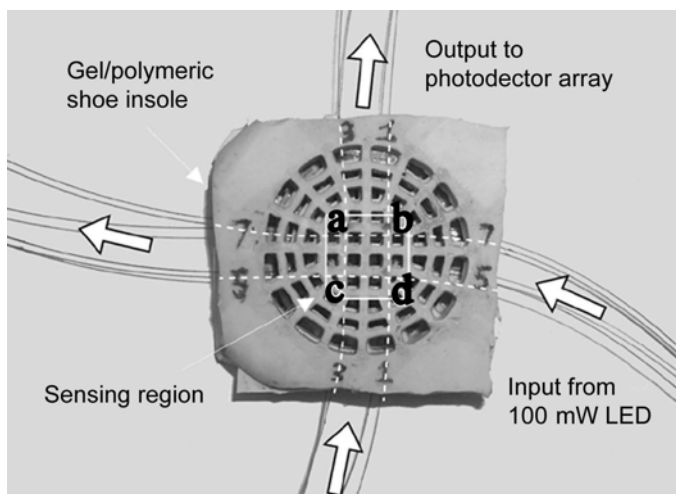


**Figure 3.** Prototype fiber-optic-sensor array; four construction lines (a, b, c, and d) show location of embedded fibers. LED = light-emitting diode.

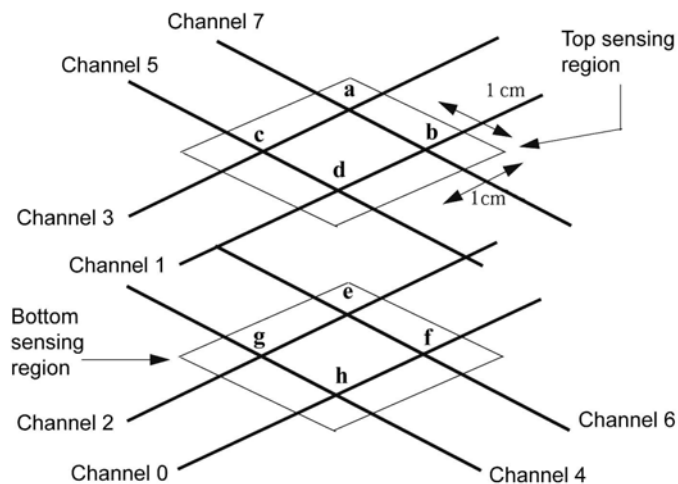


**Figure 4.** Location of each pressure point and its corresponding fiber channels.

We conducted the vertical load test using an electromagnetic materials testing device, the ELeCTroForce 3400 (EnduraTEC, Inc., Minnetonka, MN) with a 44.5 N load cell and a linear variable displacement transducer (LVDT) with a 25 mm stroke. The resolution of the device is 0.001 N and 0.0025 mm. We conducted compressive tests by placing the sensor between two planes that were in series with the actuator, LVDT, and load cell (Figure 5).

We tested each of the individual pressure points independently by applying displacements with a  $1 \times 1 \text{ cm}^2$  loading block and varying the vertical load from 0 N to

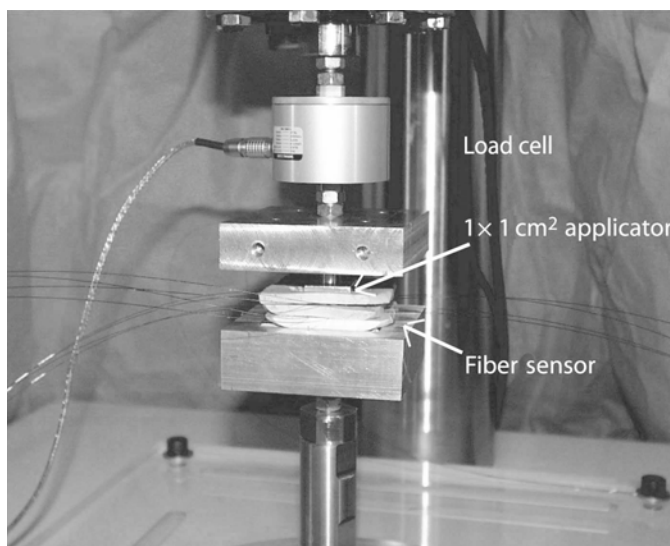


**Figure 5.** Vertical loading setup.

approximately 8.2 N (equivalent to 0 to 6 mm of displacement) at increments of 0.5 mm. After an appropriate displacement was applied, the system was allowed 30 s to equalize before we measured the applied force at 128 Hz for 5 s. We collected data continuously to ensure that the sensor was not creeping. We tested the load over all four pressure points at once with a  $2 \times 2 \text{ cm}^2$  loading plate over a vertical load range of 0 N to 26 N (again, equivalent to 0 mm to 6 mm of displacement) also using 0.5 mm displacement increments. As with compression, we applied the load for 30 s and sampled data at 128 Hz for 5 s. By dividing the total force by 4, we determined an estimate of the force experienced by each pressure point.

We conducted shear tests with a handheld force gauge, the FGE-100 (SIMPO Instrument, Itasca, IL). The gauge has a resolution of 0.1 N and can measure both compressive and tensile loads. The gauge was mounted on a manual linear translation stage (25  $\mu\text{m}$  resolution). We applied shear force to a prototype that was secured with a steel frame bracket on a  $30^\circ$  incline plane (Figure 6). We applied the load to the sensor from a rod attached to the force gauge with a  $1 \times 1 \text{ cm}^2$  pad mounted to the rod. The incremental movement of the linear stages gradually increased the load until the final load was reached. We calculated shear sensitivities on pressure point "d" as the shear force moved it toward pressure point "b" over a load of 0 N to 13.8 N at increments of 0.5 N. The loading was

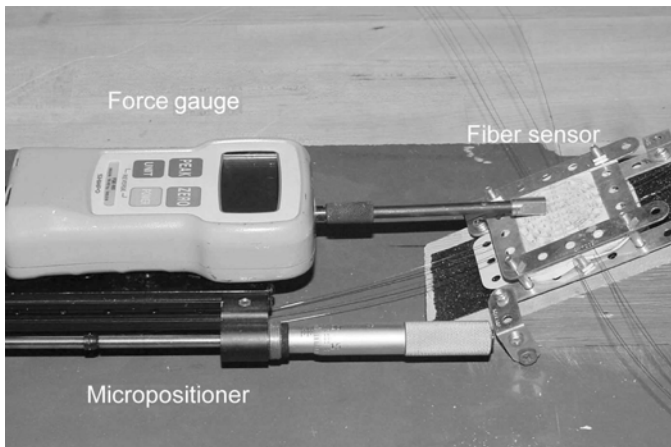


**Figure 6.**  
Shear loading setup.

applied on the sensor with a  $1 \times 1 \text{ cm}^2$  metal plate (not shown in **Figure 6**).

We constructed a map of the normal and shear stresses based on observed macrobending through the intensity attenuation from the physical deformation of fibers. To quantify the change in the sensor deformation due to the load, we generated a time history of the loading progression over the area of interest based on the intensity modulation from the corresponding fibers. We calculated the intensity curve on each pressure point on the basis of the summation of the output intensities from the two adjacent perpendicular fibers. Data obtained from the fibers were then normalized to their corresponding fiber's baseline intensity and fed into a MATLAB program to generate a three-dimensional (3-D) force map. This topographic map enables the operator to track and visualize both the movement and progression of normal and shear forces.

## RESULTS

The variation in the baseline intensity for the system was measured to be around 0.08 percent. The deviation was mainly due to the thermal-induced intensity and frequency fluctuation in the light source. We partly eliminated the intensity variation by normalizing each channel's measurement to its source intensity. We determined the applied load versus vertical displacement at the four pressure points loaded individually and all at once (**Figure 7**). The loads on the single pressure points with  $1 \times 1 \text{ cm}^2$  metal

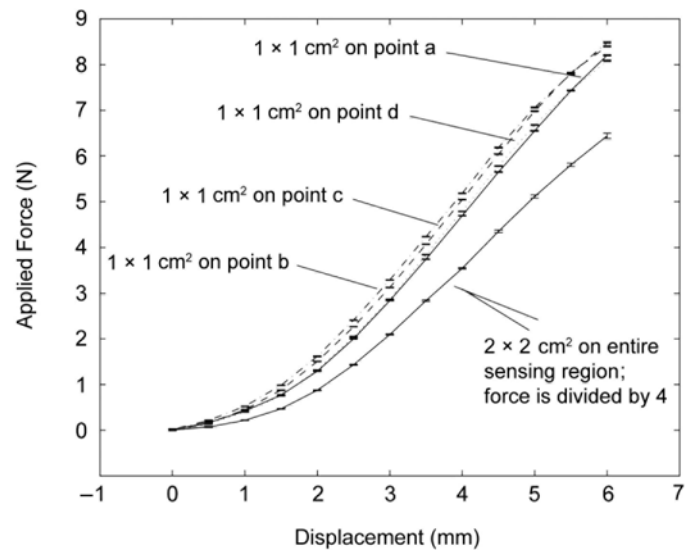


**Figure 7.**  
Force versus displacement on each pressure point.

plates were similar. The overall average standard deviation for the applied load was 0.012 N, indicating that the sensor was not creeping when the data were collected. The small discrepancies between these four curves are likely due to the uncertainties in the initialization of the zero displacement. The estimated force on each pressure point during the  $2 \times 2 \text{ cm}^2$  sensing-area load test, determined when we divide the  $2 \times 2 \text{ cm}^2$  loading data by 4, appears less than when a  $1 \times 1 \text{ cm}^2$  metal plate is used. The average standard deviation for the  $2 \times 2 \text{ cm}^2$  loading was 0.022 N, indicating no creep. The intensity of each channel varied less than 0.5 percent between multiple loadings (**Figure 8**). Multiple loadings were generated because loading each pressure point meant that the sensor layer channels were stimulated two times (e.g., channel 3 was stimulated when either point "a" or "c" was loaded). **Figure 8** shows only the top sensor layer channels that are affected by the loads. For all results hereafter, the data represent a typical measurement since the average results were not needed because very little variation occurred between trials (**Figure 8**).

The normalized intensity versus applied force of the sensor due to an applied force at point "a" demonstrated the expected intensity changes (**Figure 9(a)**). We observed light loss that was due to gradually applied forces from 0 N to 8.2 N. For channel 7, the normalized intensity change due to the load is about 13 percent, while a slightly lower intensity (8%) was observed on channel 3. As expected, channels 2 and 6, which are directly below channels 1 and 7, showed

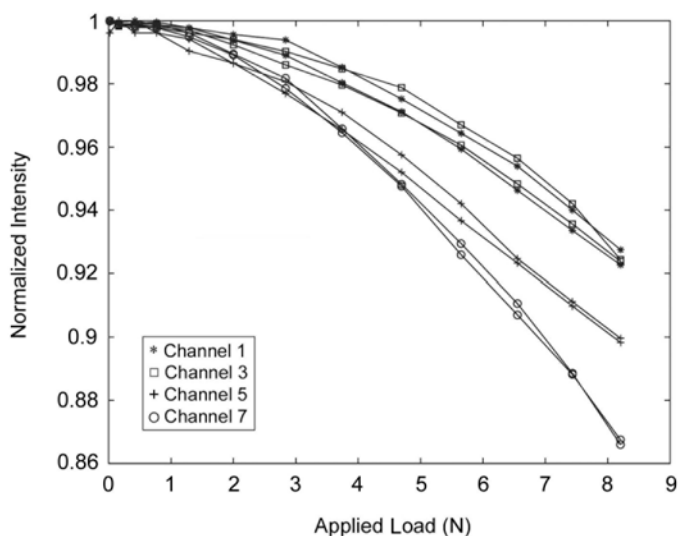


**Figure 8.** Comparison of four trials of output intensity from channels 1, 3, 5, and 7 for various vertical loads on each crossing point.

some light loss (both  $<2\%$ ) that is smaller than the top layer. Similarly, the normalized intensity versus applied force over the four sensing elements with a  $2 \times 2 \text{ cm}^2$  load plate demonstrated expected changes (**Figure 9(b)**). Here, the force on the plot is generated based on the estimated force that we determined by dividing the  $2 \times 2 \text{ cm}^2$  loading data by 4. We observed a noticeable amount of light loss on channels 1, 3, 5, and 7 that was due to a gradually increasing applied 0 N to 6.5 N normal force (or 0 N to 26 N total force). All other channels experienced smaller, but noticeable changes in intensity; why channel 6 has a noticeably larger increase than the others is not known, even though the fiber is on the bottom layer. Note: the second  $x$ -axis is the applied displacement.

We generated a topographic force map based on the force-induced intensity attenuation (**Figure 10**). The  $x$ - and  $y$ -axes are arbitrary distances representing a unit sensor length. Since our system had four channels in both the top and bottom layers, the actual fibers are indicated by the "1" and "2" on each  $x$ - and  $y$ -axis in the figure. The  $z$ -axis represents the sum of percentage intensity changes of the two crossing fibers normalized by their baseline intensity. With this map, one can see the change of the direction and magnitude of the applied load across both the top and bottom sensor layers. The information will become important in the future for gait analysis, in which the magnitude and the movement of the forces are essential.

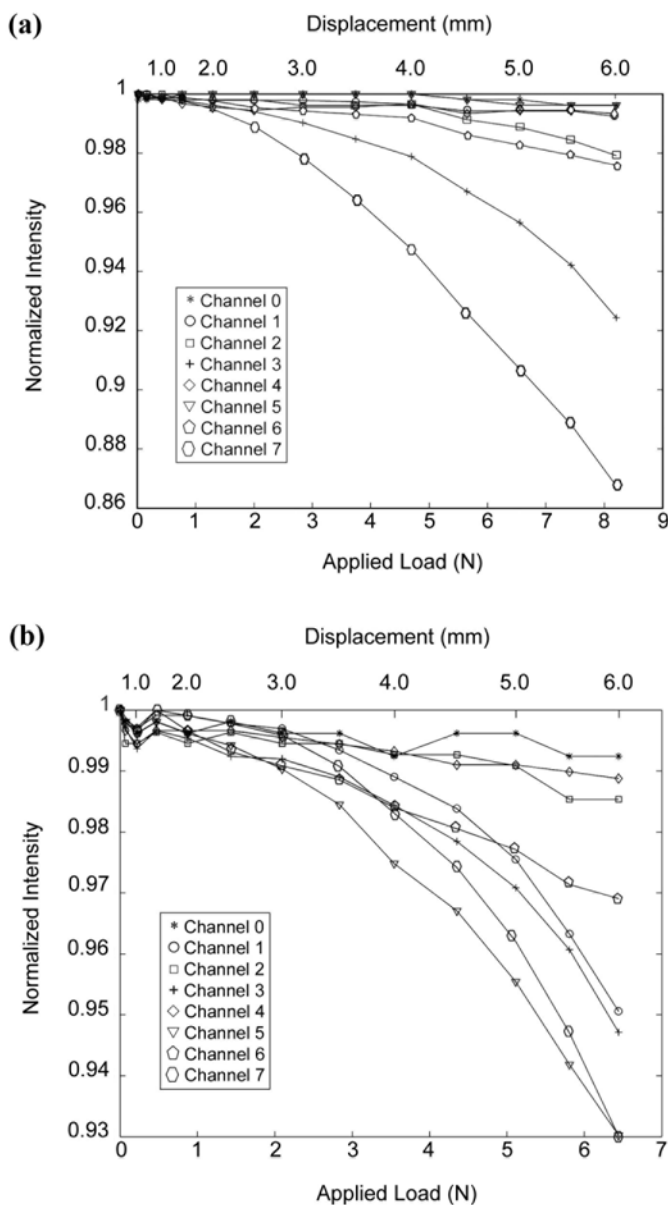


**Figure 9.** (a) Plot of output intensity versus applied force and displacement for all channels when point "a" is pressed with a  $1 \times 1 \text{ cm}^2$  applicator area and (b) plot of output intensity versus applied force and displacement for all channels when  $2 \times 2 \text{ cm}^2$  applicator area is used.

Two shear measurement trials performed on pressure point "d" demonstrated that, as expected, channels 1 and 5 had the largest change in intensity (**Figure 11**). A slight deviation exists around the heavier load region on channel 1. The deviation likely occurred because the force gauge was not securely mounted on the translation stage. The screw holding the force gauge loosened when the force

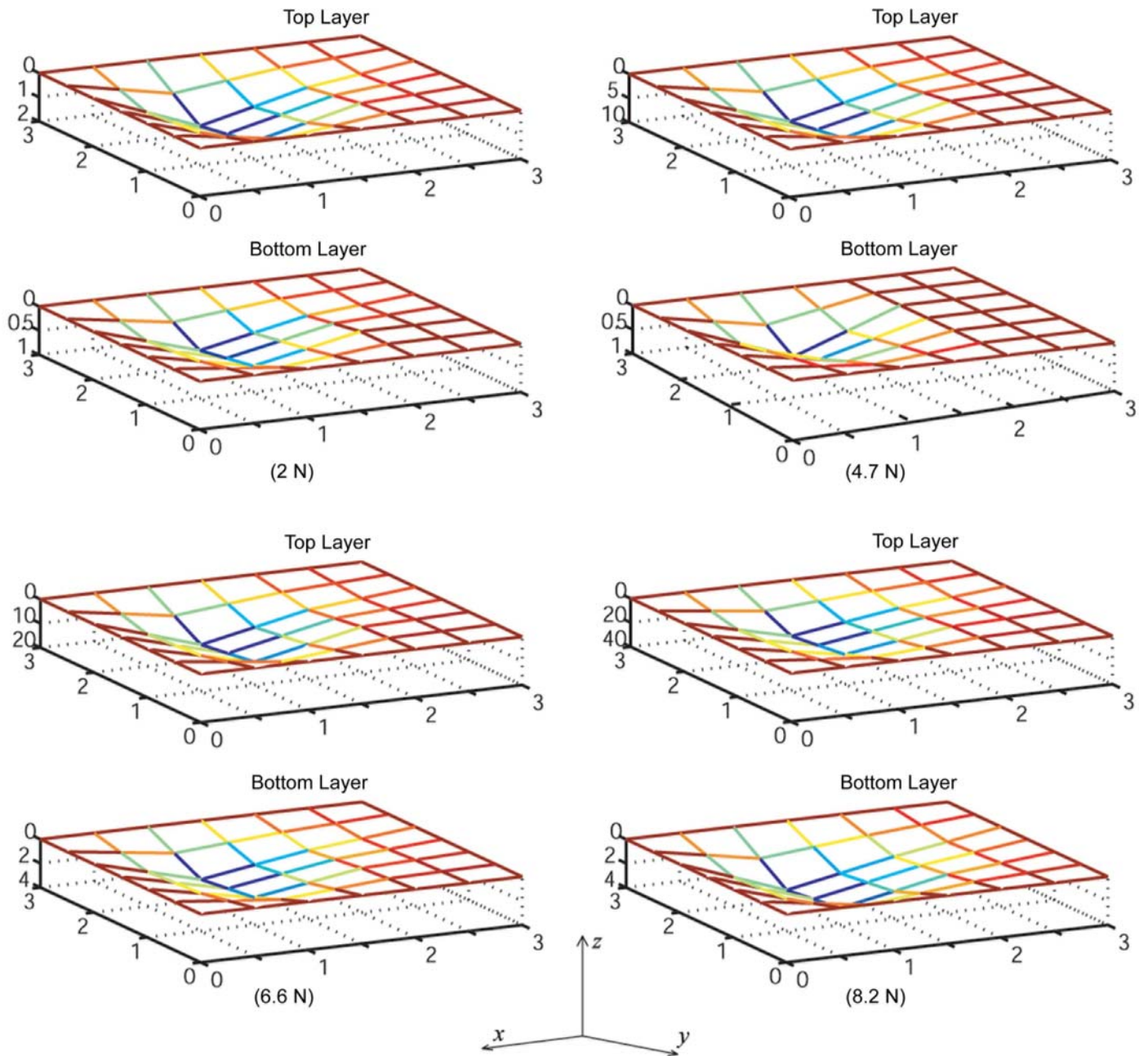


**Figure 10.**

Three-dimensional plots showing force distributions of top and bottom sensor layers due to series of loads on single point where channels intersect. (For reference, force was applied on point “a” in **Figure 4**.)  $x$ - and  $y$ -axes are arbitrary distances representing unit sensor length. Since system had four channels in both top and bottom layers, actual fibers are indicated by “1” and “2” on each  $x$ - and  $y$ -axis.  $z$ -axis represents sum of percentage intensity changes of the two crossing fibers normalized by their baseline intensity.

reached above 5 N. Holding the force gauge at a fixed position to obtain accurate loads at a pressure point became difficult.

With an applied shear force (moving point “d” toward “b” and gradually increasing from 0 N to 13.5 N),

the intensity of the fiber light changed (**Figure 12**). Both top and bottom sensors reacted to the load, and the average minimum detectable shear force was 2.2 N. Because of shearing, the location of the applied force gradually shifted from “h” toward point “f.” As the force increased,

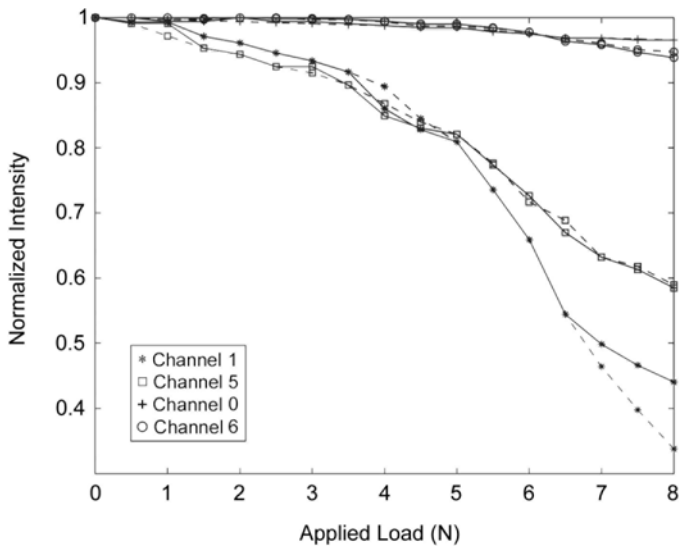


**Figure 11.** Results from two trials of output intensity from channels 1, 5, 0, and 6 for various loads applied at a pitch angle of  $30^\circ$  on point “d.”

channels 0, 4, and 6 began to bend (lose intensity); on the basis of the sensor design, these were the bottom layer channels that we expected to change (**Figure 4**).

We generated a topographic force map based on the observed light-intensity attenuation from shear forces (**Figure 13**). We observed a noticeable deflection from point “d” to “b” and from point “h” to “f” when the applied shear force was near 8 N. Force image curves show the vertical load shifting from one location to another on the top and bottom layers.

## DISCUSSION

Comparing the  $1 \times 1 \text{ cm}^2$  data and  $2 \times 2 \text{ cm}^2$  data demonstrated that for the same displacement, a larger force per unit area was generated with the  $1 \times 1 \text{ cm}^2$  application (**Figure 7**). One probable reason for the larger force can be explained if one considers edge effects; that is, the sum of the total effective area of four individual  $1 \times 1 \text{ cm}^2$  applicators is larger than a single  $2 \times 2 \text{ cm}^2$  applicator. Therefore, the  $2 \times 2 \text{ cm}^2$  applicator has a smaller load per unit area for the same displacement.

Similarly, the intensity changes seen with the  $1 \times 1 \text{ cm}^2$  applicator did not match those seen with the same channels and a  $2 \times 2 \text{ cm}^2$  applicator (e.g., channels 3 and 7 in **Figure 9(a)** and **(b)**). (Note: although the applied forces were different, the displacements were the

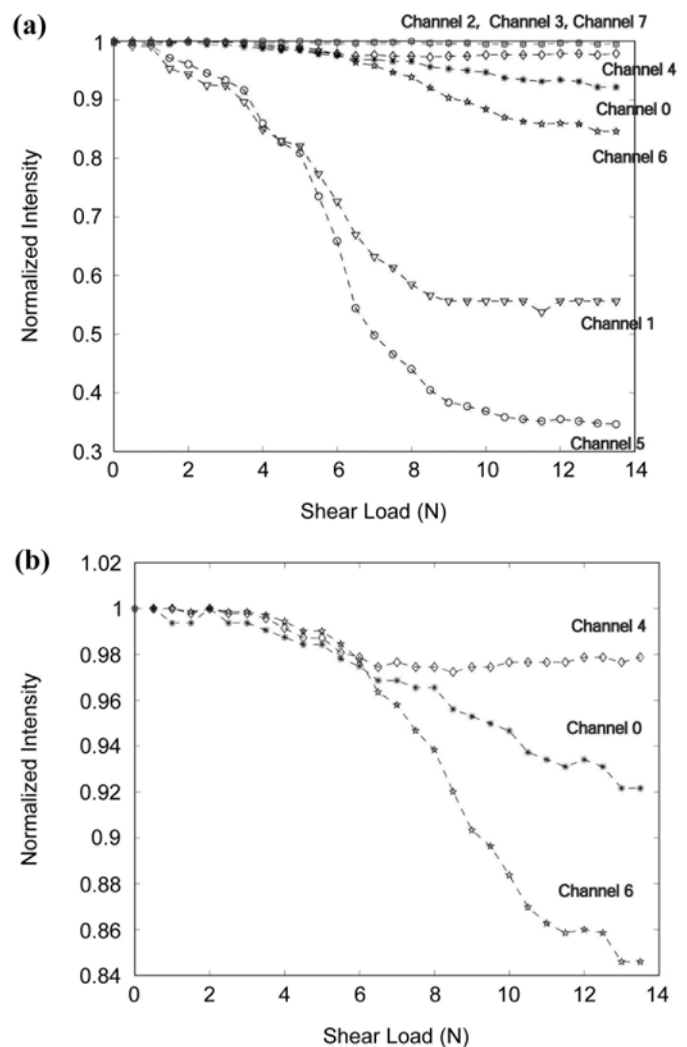


**Figure 12.** (a) Output intensity versus applied force at  $30^\circ$  pitch angle on point “d” as it moves toward “b”; (b) close-up of (a).

same.) After closer inspection, we found that the difference in the load curve occurs because the smaller bending radius  $R$  associated with concentrated loads in a smaller area has a higher bend loss than a more widely distributed load that has a larger bend radius. The equation in “Methodology” shows that when  $R$  increases, the attenuation decreases. Since a smaller applicator created a smaller bending radius on the fibers than a bigger plate, the loss will be greater. This is most likely why the intensity does not match between two different load areas. On the basis of the results, we conclude that we will not be able to calibrate this sensor with this method because we could not load each sensor independently.

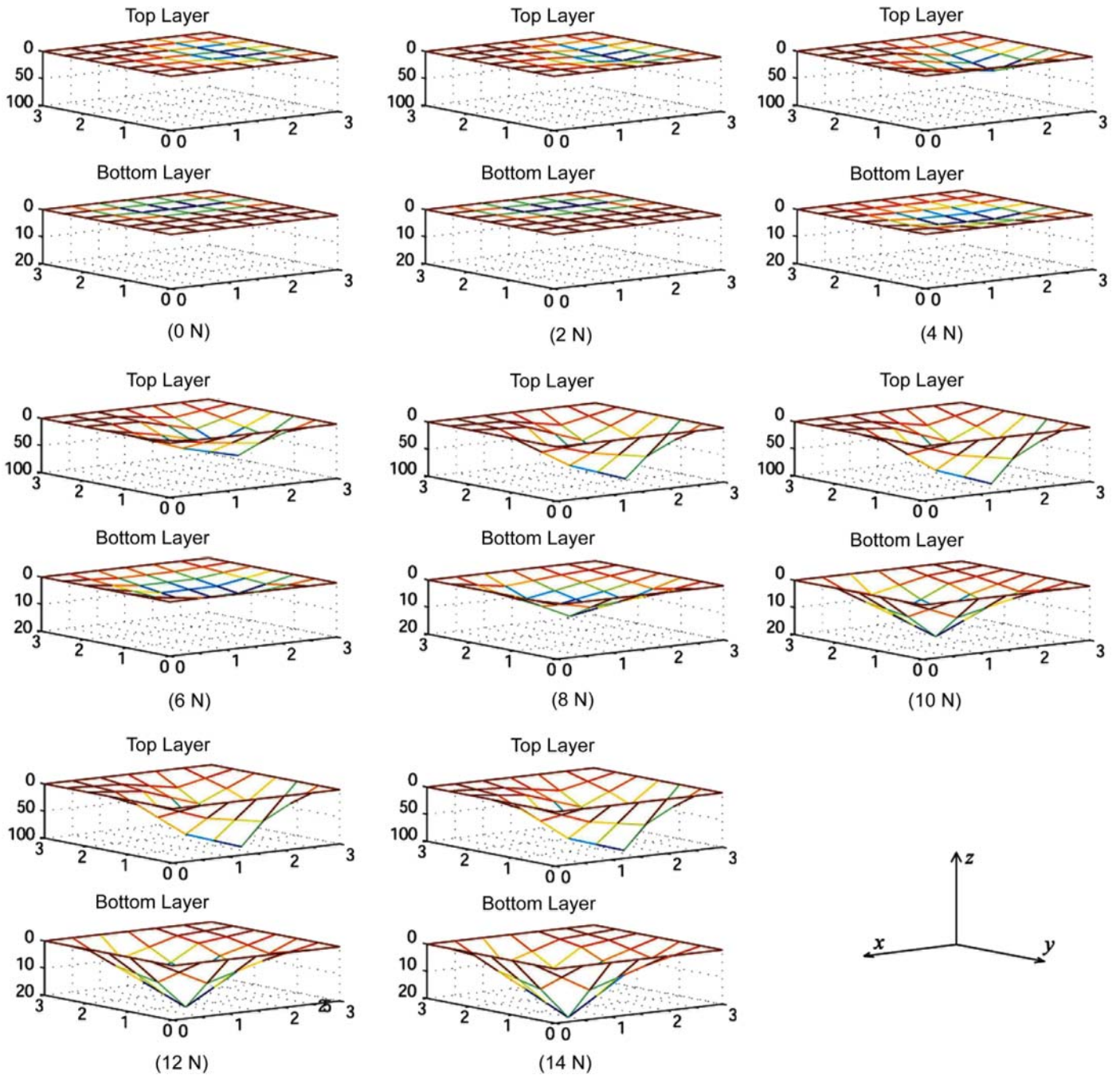


**Figure 13.**

Time evaluation of shear loading on top and bottom sensor layers due to series of applied loads. Loads ranged from 0 N to 13.5 N and were applied at a pitch angle of  $30^\circ$  as point “h” moves toward “f.” As in **Figure 10**,  $x$ - and  $y$ -axes are arbitrary distances representing unit sensor length. Since system had four channels in both top and bottom layers, actual fibers are indicated by “1” and “2” on each  $x$ - and  $y$ -axis.  $z$ -axis represents sum of percentage intensity changes of the two crossing fibers normalized by their baseline intensity.

Overall, the sensor’s performance was consistent. From the results from **Figure 8**, one can see that the intensity responses of four fiber channels on the top sensor

layer loaded at four different locations follow almost the same curves. This result is quite good since the fibers are secured to the elastomeric pad only by strings. The

slightly larger deviation on channels 1 and 3 between different single pressure-point trials is likely due to a drift in the baseline intensities of these two channels. The average deviation in both channels is around 0.5 percent. The baseline problem can be resolved if one uses tap (reference) fiber detectors that monitor fluctuations in input intensity and normalizes the outputs to the tap intensity.

The sensor required an arbitrary 30 s waiting period after the load was applied so that any effect from creep would be avoided. Future sensors will use materials that have a more rapid response to applied loads.

Other minor improvements can be made to improve the sensitivity variation between each fiber channel (**Figure 9(b)**). In this experiment, the response appeared to be greater for channels 5 and 7, while channels 1 and 3 appeared to have a similar but weaker intensity response from the loads. The deviation is likely attributed to a lack of precision from the manual assembly of the prototype. The input-light coupling was one of the biggest concerns. Because of a lack of precise alignment between the fiber and the LED input, each fiber receives different amounts of light. The coupling effect affects the amount of light reduction that occurs. The variation in the detectors' responsivity also comes from the variation in the output intensity. This variation occurs because some small variation always exists in the quantum efficiencies and nominal operating wavelengths of the detectors. This variation also likely occurs because the fibers are imprecisely mounted to the embedded material and the loading area is not perfectly aligned with some of the fibers. This problem has been resolved with the use of a microfabricated waveguide structure [16–17]. Before one can correctly create a pressure or strain map based on the observed macrobending through intensity attenuation from the fibers, one must resolve the problems in bending radiuses created by different-size loading areas. Despite these problems, one can still generate a 3-D force map of a force applied on a single pressure point (**Figure 10**). For the shear measurements, the shear and normal forces were constructed based on the observed macrobending through the intensity attenuation of the fibers from both layers of the sensor (**Figure 13**). Overall, both plots clearly identify the magnitude of the load and the direction of the load in progression.

## CONCLUSION

This paper investigates the potential of measuring localized plantar pressure and shear with a fiber-optic sensor array. Because of edge effects during loading, calibrating the sensor was not possible; i.e., we could not use the  $1 \times 1 \text{ cm}^2$  intensity versus force relationship to calculate the force from intensity changes during the  $2 \times 2 \text{ cm}^2$  loading. However, we are currently working on a prototype in which a microbend structure will be implemented into the sensor structure. The design will have a predefined bending pattern with the use of a corrugated structure; therefore, the fiber will bend according to the contour of the deformer and not by the curvature of the load plate. The bend loss then becomes a function of the displacement and is independent of the load plate's size. The light attenuation can be made close to linear with an optical switching design described by Lawson and Tekippe [18]. We will discuss the result of this new implementation in an upcoming publication. Other results from the pressure and shear tests were encouraging. The change in light intensity was repeatable in compression and shear. We demonstrated that pressure and shear, in addition to magnitude and direction of an applied force, can cause noticeable changes in two-layer macrobend fiber-optic sensor arrays.

## REFERENCES

1. Sumpio BE. Foot ulcers. *N Engl J Med*. 2000;343(11):787–93.
2. Cavanagh P, Ulbrecht JS, Capulo GM. The biomechanics of the foot in diabetes mellitus. In: Bokwer, JH, Pfeifer MA, editors. *The diabetic foot*. St. Louis (MO): C.V. Mosby; 2001. p. 125–96.
3. Boulton AJ, Hardisty CA, Betts RP, Franks CI, Worth RC, Ward JD, Duckworth T. Dynamic foot pressure and other studies as diagnostic and management aids in diabetic neuropathy. *Diabetes Care*. 1983;6(1):26–33.
4. Veves A, Murray HJ, Young MJ, Boulton AJ. The risk of foot ulceration in diabetic patients with high foot pressure: a prospective study. *Diabetologia*. 1992;35(7):660–63.
5. Brand PW. Repetitive-stress in the development of diabetic foot ulcers. In: Levin ME, O'Neal LW, editors. *The diabetic foot*. St. Louis (MO): C. V. Mosby; 1988. p. 83–90.
6. Delbridge L, Ctercteko G, Fowler C, Reeve TS, Le Quesne LP. The aetiology of diabetic neuropathic ulceration of the foot. *Br J Surg*. 1985;72(1):1–6.
7. Habershaw GM, Chzran J. Biomechanical considerations of the diabetic foot. In: Kozak GP, editor. *Management of*

- diabetic foot problems. Philadelphia (PA): W.B. Saunders; 1995. p. 53–65.
8. Jenkin WM, Palladino SJ. Environmental stress and tissue breakdown. In: Frykberg RG, editor. *The high risk foot in diabetes mellitus*. New York (NY): Churchill Livingstone; 1991. p. 103–23.
  9. Lord M, Hosein R, Williams RB. Method for in-shoe shear stress measurement. *J Biomed Eng*. 1992;14(3):181–86.
  10. Tappin JW, Pollard J, Beckett EA. Method of measuring “shearing” forces on the sole of the foot. *Clin Phys Physiol Meas*. 1980;1(1):83–85.
  11. Akhlaghi F, Pepper MG. In-shoe biaxial shear force measurement: the Kent shear system. *Med Biol Eng Comput*. 1996;34(4):315–17.
  12. Christ P, Gender M, Seitz P. A 3-D pressure distribution measuring platform with  $8 \times 8$  sensors for simultaneous measurement of vertical and horizontal forces. VI EMED Scientific Meeting, Dinh B, editor. 1998 Aug 8–12. Brisbane (Australia): Proceedings of VI EMED Scientific Meeting; 1998. p. 120–25.
  13. Davis BL, Perry JE, Neth DC, Waters KC. A device for simultaneous measurement of pressure and shear force distribution on the plantar surface of the foot. *J Appl Biomech*. 1998;14(1):93–104.
  14. Udd E. *Fiber optic sensors*. New York (NY): John Wiley & Sons, Inc.; 1990. p. 1–10.
  15. Wolf HF. *Handbook of fiber optics: theory and applications*. New York (NY): Garland STPM Press; 1979. p. 44–152.
  16. Wang W-C, Panergo R, Galvanin C, Ledoux W, Sangeorzan B, Reinhall P. A flexible micromachined optical sensor for simultaneous measurement of pressure and shear distribution on foot. 2003 SPIE NDE health monitoring and diagnostics. 2003 Mar 2–7; San Diego (CA). Bellingham (WA): SPIE 5047; 2003. p. 275–85.
  17. Wang W-C, Panergo R, Ledoux W, Sangeorzan B, Reinhall P. A PDMS based distributive shear/pressure sensor, Mesher A, editor. Proceedings of the 12th International Polymer Fiber Conference. 2003 Sept 14–17; Seattle (WA). Washington (DC): Optical Society of America; 2003. p. 68–71.
  18. Lawson CM, Tekippe VJ. Environmentally insensitive diaphragm reflectance pressure sensor, Kundu T, editor. 1983 SPIE Fiber Optic and Laser Sensors. 1983 Apr 5–7; Arlington (VA). Bellingham (WA): Proc. SPIE 412; 1983. p. 96–103.

Submitted for publication July 1, 2004. Accepted in revised form January 6, 2005.